Journal of Materials Chemistry C

ROYAL SOCIETY OF CHEMISTRY

COMMUNICATION

View Article Online
View Journal | View Issue

Cite this: J. Mater. Chem. C, 2024, 12, 13236

Received 13th May 2024,
Accepted 2nd August 2024

DOI: 10.1039/d4tc01967a

rsc.li/materials-c

Single crystal synthesis and surface electronic structure of $Bi_{1.993}Cr_{0.007}Se_3$†

Sandra Gardonio, *[a] Zipporah Rini Benher, [a] Mattia Fanetti, [a] Paolo Moras, [b] Polina M. Sheverdyaeva [b] and Matjaz Valant [a]

Topological insulators containing single atoms of magnetic metals are useful for studying the effects of magnetism on the topological properties of matter. Controlling the distribution of magnetic atoms remains a major issue during the synthesis of these materials, as the formation of clusters and/or unwanted precipitates competes energetically with the formation of dilute phases. Here, we report the synthesis of large Bi_2Se_3 single crystals with rhombohedral structure and extremely low concentration (0.15 at%) of substitutional Cr ions using the Bridgman method. After exfoliation, the crystals exhibit a topological surface state with an energy-momentum dispersion different from that of pristine Bi_2Se_3, due to the presence of an apparent energy gap at the Dirac point. The properties of this state are discussed in comparison with previous spectroscopic measurements of Cr-doped Bi_2Se_3 films.

The synthesis of magnetic topological insulator (TI) materials and their topological electronic structures and magnetic properties are currently the subject of intense research activities.[1]

TIs in three dimensions are characterized by gapless surface states with linear (Dirac-like) energy-momentum dispersion, if the time-reversal symmetry is preserved. These topological surface states (TSSs) originate from the bulk band inversion induced by strong spin–orbit interactions. Bi_2Se_3, Bi_2Te_3 and Sb_2Te_3 are prototypical bulk materials that exhibit TSSs and have attracted much attention in the fields of photodetectors, field-effect transistors, energy conversion and storage, and catalysis.[2–8] In particular, it is predicted that the interplay of magnetism and topology can lead to remarkable phenomena, such as the quantum anomalous hall effect, which could have major implications in the field of spintronics.[9] Theoretical and experimental advances have been made towards a comprehensive description of the behavior of topological magnetic materials.[1,10] However, the effect of diluted magnetic dopants on the electronic structure of a TI is still not fully understood.

TSS are exceptionally sensitive to perturbations breaking the time-reversal symmetry, such as magnetic fields or magnetic moments localized on the surface.[11] Theory predicts that a single magnetic impurity on the surface of a TI can induce a gap opening in the local density of states.[12] A TI with randomly distributed magnetic impurities should be gapped everywhere, at least at the mean-field level.[12] An experimental verification of these scenarios is challenging from a materials perspective. Random magnetic impurities can be produced either by deposition of minute quantities of magnetic elements on the TI surface or by embedding magnetic dopants during the synthesis of the TI materials. The first approach requires low temperatures to limit the thermal diffusion of magnetic atoms on the surface and suppress the aggregation of isolated atoms into clusters and/or islands. The second approach allows to introduce diluted impurities during the synthesis of TI single crystals or thin films, which can be studied even at room temperature. However, also in this case, aggregation of the magnetic dopants could occur, depending on the solubility limit of the dopant and the growth procedures.

The solubility of magnetic of 3d transition metals in prototypical TIs is very low. An exemplary case is the Cr-doped Bi_2Se_3.[13] To date, major efforts to understand the properties of TI doped with dilute magnetic impurities have been pursued in thin films grown by molecular beam epitaxy (MBE), such as $Bi_{2-x}Cr_xSe_3$ thin films. Up to a Cr content of $x = 0.05$, $Bi_{2-x}Cr_xSe_3$ films showed good crystalline quality.[14–16] The most energetically favorable process to achieve Cr doping is the Bi substitution.[15,17] The formation of large defect complexes with Cr atom pairs at substitutional and interstitial sites was found theoretically and experimentally to be more favorable for Cr contents of $0.02 < x < 0.40$.[15,18] Studies of the magnetic properties of Cr-doped Bi_2Se_3 films[14,15,19] showed a ferromagnetic behavior at low temperature, with a magnetic moment of about $\sim 2\mu_B$ per Cr ion and Curie temperature T_C that depends on the dopant concentration.[15,19–21] X-ray

[a] Materials Research Laboratory, Univerza v Novi Gorici, Vipaska 11c, Ajdovščina 5270, Slovenia. E-mail: sandra.gardonio@ung.si
[b] CNR-Istituto di Struttura della Materia (CNR-ISM), S.S. 14, km 163.5, I-34149 Trieste, Italy

† Electronic supplementary information (ESI) available. See DOI: https://doi.org/10.1039/d4tc01967a

absorption spectroscopy showed that Cr dopants exhibit a +2 oxidation state when they replace trivalent Bi atoms in the Bi_2Se_3 matrix.[16] This result was associated with the covalent character of the Cr–Se bond and the observed local structural relaxation of the Bi_2Se_3 lattice.[16] The effects of Cr doping on the TSS of Bi_2Se_3 films were investigated by angle-resolved photoelectron spectroscopy (ARPES), which pointed out a band gap opening at the Dirac point of the TSS.[18,22–24] The origin of the gap is still controversial; some studies attribute the gap to ferromagnetic ordering,[22] while others argue that it is due to the resonance states of impurities.[25] In this context, the study of bulk Bi_2Se_3 crystals, in which the Cr dopants are diluted to thermodynamic solubility and more uniformly distributed than in MBE-grown films, could shed light on the origin of the gap opening in TSSs.

Growing from a molten phase is an alternative method to MBE that enables the growth of macroscopically large, high-quality TI crystals.[26] In a previous study dealing with the preparation of single crystals by the Bridgman method starting from the nominal mixture $Bi_{2-x}Cr_xSe_3$ with $0.005 \leq x \leq 0.04$ (*i.e.* low content of Cr in the starting mixture) the solid solubility of Cr at 600 °C was determined to be below $x = 0.02$.[27] Secondary phase nano-precipitates of $Bi_2Cr_4Se_9$ were detected for $x > 0.02$. The low solubility of Cr in Bi_2Se_3 is advantageous as it allows to study the effects of the magnetic impurities on the topological properties, without affecting the intrinsic bulk properties of the TI (*i.e.* by introducing extrinsic charge carrier concentration, *etc.*). From the point of view of the melt synthesis using conventional laboratory equipment, however, this is a challenge, as the preparation of stoichiometric mixtures with amounts of Cr below its solid solubility in Bi_2Se_3 is at the limit of the experimental precision and reproducibility. As soon as the Cr content exceed the solid-state solubility, the formation of precipitates of secondary phases in the matrix is unavoidable. One strategy to overcome the problem, here adopted, is to determine the optimized processing regime,[28] in order to avoid the formation of the nano precipitates within the Bi_2Se_3 matrix. We allow for the growth of large crystalline secondary phases that can be easily separated from the Bi_2Se_3 matrix. At the end of the process, precise control of the composition is achieved: the matrix is saturated with the Cr magnetic dopants, while large crystalline precipitates of the secondary phases are completely separated from the matrix. It is important to notice that within the Cr-saturated Bi_2Se_3 matrix the homogeneous distribution of the magnetic dopants is thermodynamically favored because every departure from homogeneity causes local instability due to local excess of the solid solubility limit.

The preparation of the material, following the strategy described above, was done based on the available phase diagram for the Bi_2Se_3–Cr_2Se_3 join of the ternary system Bi–Cr–Se.[13]

Bismuth and selenium (99.9%) were purchased from Sigma Aldrich. Chromium (99.999%) was purchased from MaTeck GmbH. A mixture of metals corresponding to Bi : Cr : Se = 1.85 : 0.15 : 3.00 was sealed in an evacuated quartz ampoule. The Cr content was significantly above its solubility limit in Bi_2Se_3 and lied within the $Bi_2Cr_4Se_9$ phase field.

To obtain a homogeneous melt, the ampoule was heated up to 1000 °C at 40 °C h^{-1} and kept at this temperature for 48 h. The temperature was then slowly lowered to 250 °C at 5 °C h^{-1}. During the cooling the system went through $Bi_2Cr_4Se_9$ phase field where $Bi_2Cr_4Se_9$ crystals formed and grow. Due to the very slow cooling rate they grew to a significant size of about 250 μm. By further cooling the system entered into the Bi_2Se_3 phase field causing crystallization of large flake-like Bi_2Se_3 crystals saturated with Cr. Our post-growth analysis by X-ray diffraction (XRD) and energy dispersive X-ray spectroscopy (EDX) allowed us to identify and localize the different phases in the synthesized ingots. Within our detection constraints, we found that the Cr ions are dilute and homogeneously distributed in the matrix of large single crystals of Bi_2Se_3. To control the material obtained from supersaturated compositions, we also analyzed the material obtained from a starting mixture Bi : Cr : Se = 1.95 : 0.05 : 3.00, and we obtained similar XRD, SEM and EDX results as for the starting composition Bi : Cr : Se = 1.85 : 0.15 : 3.00.

The effects of Cr doping on the TSS, probed by ARPES, are consistent with previous studies on Cr-doped Bi_2Se_3 films,[23,24,29] grown by MBE, where the opening of an apparent energy gap was observed. Therefore, the results shown here indicate a viable way to synthesize bulk TIs doped with magnetic elements.

The XRD pattern of the powdered samples was collected with a Rigaku Miniflex600 diffractometer. Microscopy analysis was performed with a field-emission scanning electron microscopy (SEM) (Jeol JSM-7100F) equipped with back-scattered electron detector and operated at 15 kV. The chemical composition was determined by fitting the EDX spectra measured with an Oxford XMax-80 spectrometer (with Aztech acquisition and analysis software) installed on the same SEM. The photoemission experiments were carried out at Elettra synchrotron (Trieste, Italy) on clean surfaces obtained by cleaving the samples *in situ* in ultra-high vacuum with pressure lower than 1.2×10^{-10} mbar. Low energy electron diffraction (LEED) was used to monitor the surface crystalline structure of the samples. The X-ray photoelectron spectroscopy (XPS) and ARPES experiments were carried out at a VUV-Photoemission beamline (Elettra, Trieste) using a Scienta R4000-WAL hemispherical electron energy analyser mounted at 45° to the beam direction. The XPS spectra were measured using a photon energy of 700 eV with a total energy resolution of ~200 meV and the ARPES maps were measured at a photon energy of 45 eV with *p*-polarized light and with an energy resolution of ~10 meV. XPS and ARPES measurements were acquired on the sample kept at room temperature. The XPS spectra were fitted with Voigt spin–orbit doublets and Shirley-type background was subtracted. The fitting parameters used for the Bi 5d and Se 3d core level spectra are reported in Table S1 (ESI†).

To gain an insight into the phases present in the solid ingot, the XRD pattern (Fig. 1) was measured on a sample obtained by pulverizing crystallites from different parts of the ingot. A photographic description of the ingot can be found in Fig. S1 (ESI†). The XRD pattern shown in Fig. 1 provides information on the structure of the phases present in polycrystalline ingot with nominal composition $Bi_{1.85}Cr_{0.15}Se_3$.

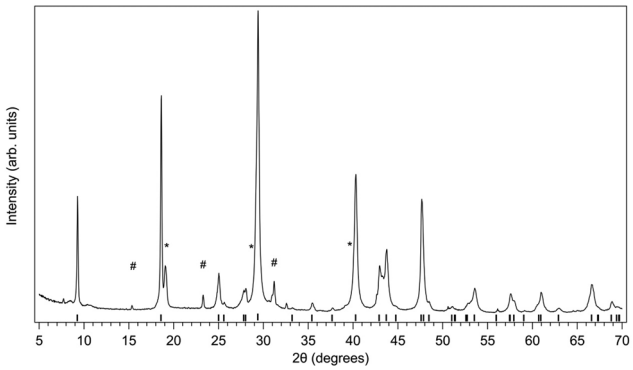

Fig. 1 Powder XRD pattern measured on a sample obtained by pulverizing crystallites from different parts of the ingot with nominal composition $Bi_{1.85}Cr_{0.15}Se_3$. The reference patterns of Bi_2Se_3 (bars) and some selected diffraction peak of $Bi_2Cr_4Se_9$ (hashtags) and BiSe (stars) corresponding to PDF #00-033-021, PDF #00-050-1436, and PDF #00-042-1045, respectively, are shown.

The observed XRD pattern originates mainly from a rhombohedral structure close to Bi_2Se_3 with additional diffraction peaks of triclinic $Bi_2Cr_4Se_9$ and hexagonal intermetallic BiSe.

Fig. 2(a) and (b) display backscattered electron images of different regions of the ingot. Most of the ingot consists of flat and chemically homogeneous areas exceeding 500 μm × 500 μm, as shown in Fig. 2(a). The EDX analysis of these areas (green spectrum in Fig. 2(c)) gives the chemical composition in at % as 40.85% Bi, 0.15% Cr and 59% Se. We identify them with the prevalent Bi_2Se_3-like phase detected by XRD and, therefore, with $Bi_{1.993}Cr_{0.007}Se_3$ single crystals. In some regions of the ingot (Fig. 2(b)), two minor phases are also visible. The blue rectangle in Fig. 2(b) encloses a phase with chemical composition 13.95% Bi, 27.6% Cr and 58.45% Se (blue EDX spectrum in Fig. 2(c)), corresponding approximately to $Bi_2Cr_4Se_9$. The other minor phase contains about 20 at % of Cr substituting Bi (red EXD spectrum in Fig. 2(c)) and is identified with the intermetallic $BiCrSe_3$ compound. Occasionally, large $Bi_2Cr_4Se_9$ crystals of about 250 μm × 250 μm are observed (Fig. S2, ESI†), while the mean grain size of $BiCrSe_3$ is about 10 μm × 10 μm.

Overall, these analyses demonstrate that in the predominant $Bi_{1.993}Cr_{0.007}Se_3$ phase, Cr is diluted to a concentration corresponding to its solid solubility limit.[27] The applied heat treatment resulted in complete phase separation and excludes the presence of precipitates of the two minor phases in the Bi_2Se_3 matrix. Synthesis performed with a nominal Cr content close to the solubility limit of Cr in Bi_2Se_3 (*e.g.* $Bi_{2-x}Cr_xSe_3$ with $0.005 \leq x \leq 0.04$), were found to behave differently[27] as the phase-separated regions were small and difficult to isolate from Cr-doped Bi_2Se_3.

Our growth method allowed us to obtain $Bi_{1.993}Cr_{0.007}Se_3$ samples with homogeneously distributed Cr atoms and sufficiently large lateral size to analyze their surface properties by conventional, *i.e.* space-averaging, LEED and photoemission spectroscopies.

The hexagonal pattern observed by LEED on vacuum-cleaved $Bi_{1.993}Cr_{0.007}Se_3$ is consistent with the rhombohedral crystal

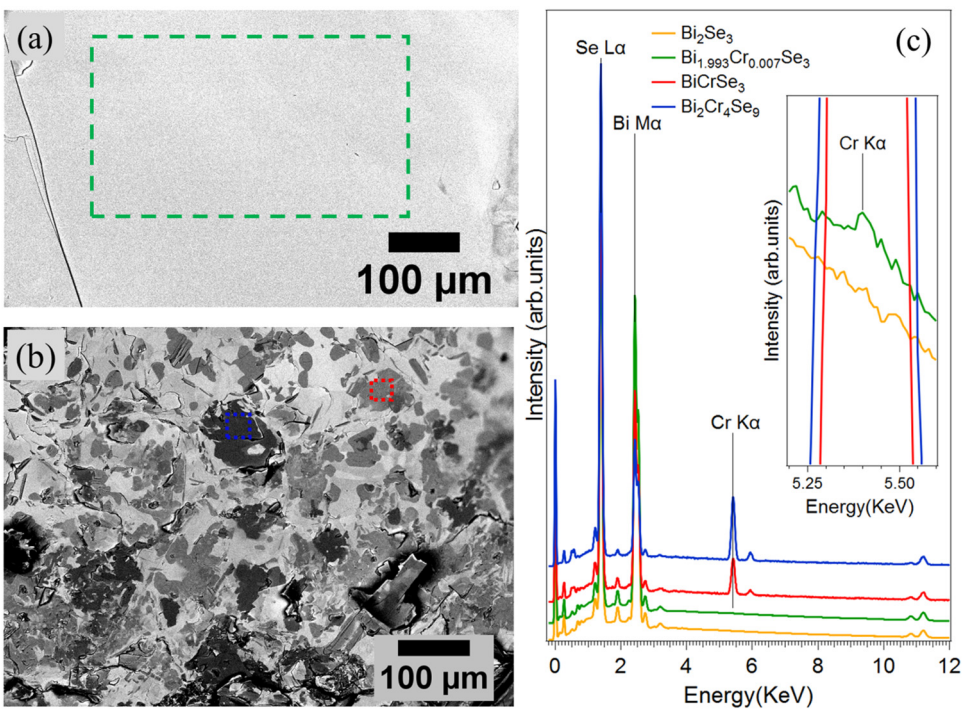

Fig. 2 Backscattered electron image of (a) a large region of the prevailing $Bi_{1.993}Cr_{0.007}Se_3$ phase (green) and of (b) the minor phases. (c) EDX spectra measured within the rectangles of panels (a) and (b) on the $Bi_{1.993}Cr_{0.007}Se_3$ (green), $BiCrSe_3$ (red) and $Bi_2Cr_4Se_9$ (blue) phases. The EDX spectrum of Bi_2Se_3 is reported as a reference. Inset: Zoom of the EDX spectra in the energy range of the Cr Kα emission line showing the difference between $Bi_{1.993}Cr_{0.007}Se_3$ and Bi_2Se_3.

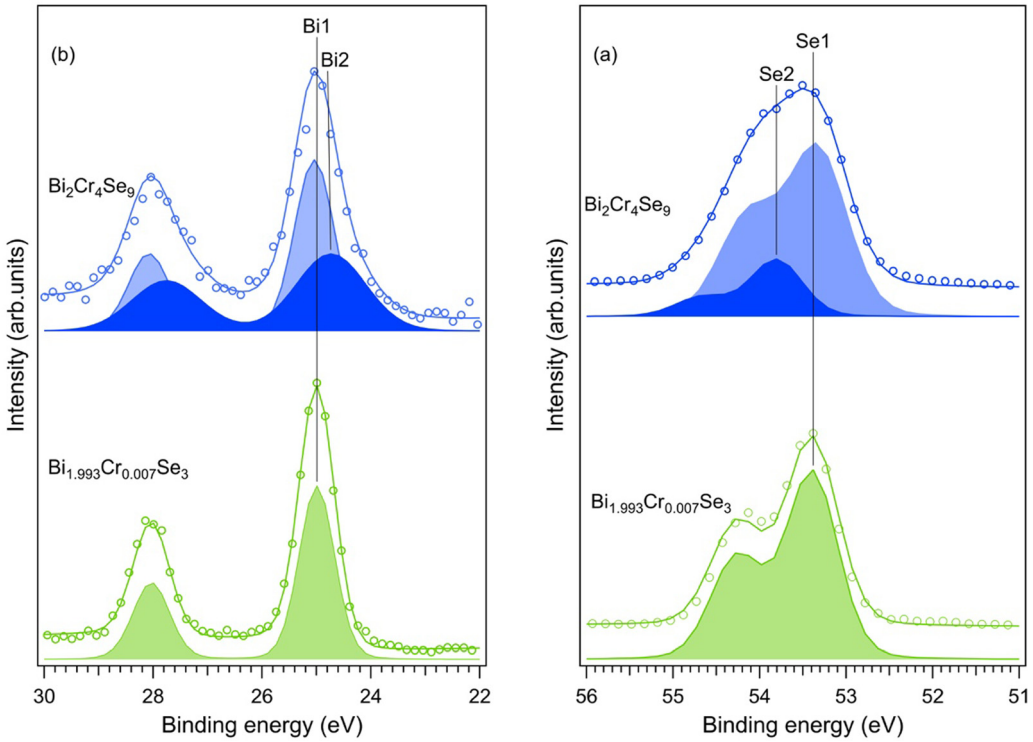

Fig. 3 (a) Se 3d and (b) Bi 5d core level spectra measured on $Bi_{1.993}Cr_{0.007}Se_3$ and $Bi_2Cr_4Se_9$ with photon energy, $h\nu$ = 700 eV. The fitting of the curves using the fitting parameters reported in Table S1 (ESI†). The spectra are normalized to the maximum peak intensity.

structure (Fig. S3, ESI†). Fig. S4 (ESI†) shows the core level spectra measured on $Bi_{1.993}Cr_{0.007}Se_3$, pure Bi_2Se_3 and the $Bi_2Cr_4Se_9$ phase. No signature of carbon or oxygen contamination was found. Importantly, the concentration of Cr in $Bi_{1.993}Cr_{0.007}Se_3$ phase is so low that Cr 2p and Cr 3p core levels are not detected,[23] while they are readily visible in a crystallite of the $Bi_2Cr_4Se_9$ phase.

The Bi 5d and Se 3d core level spectra of $Bi_2Cr_4Se_9$ and $Bi_{1.993}Cr_{0.007}Se_3$ measured by XPS are reported in Fig. 3.

The Bi 5d levels (Fig. 3(b)) show that the Bi1 component of the $Bi_2Cr_4Se_9$ and $Bi_{1.993}Cr_{0.007}Se_3$ phases has binding energy (BE) 25 eV, which is comparable to the BE of pure Bi_2Se_3 (Fig. S5, ESI†). The Bi 5d of the $Bi_2Cr_4Se_9$ phase shows also the Bi2 component at 150 meV lower BE than the Bi1 component, which is not detected in the $Bi_{1.993}Cr_{0.007}Se_3$ phase. Bi2 cannot correspond to metallic Bi which is expected at about 1 eV lower BE than Bi1, according to ref. 23. Instead, it can originate from Bi atoms of the compound having lower oxidation state than the +3.[30] The core level spectra of Se 3d (Fig. 3(a)) show the Se1 component at 53.3 eV in both $Bi_{1.993}Cr_{0.007}Se_3$ and $Bi_2Cr_4Se_9$ phases, similarly to Bi_2Se_3 (Fig. S5, ESI†). The addition of a Se2 component with BE 53.8 eV is necessary for the fitting of $Bi_2Cr_4Se_9$. It is plausible to assume that the Se2 component is due to Se atoms having higher oxidation state than −2.[30–32] The absence of the Se2 component in the case of $Bi_{1.993}Cr_{0.007}Se_3$ confirms the absence of Cr-rich precipitates on its surface. Formation energies calculation[17] and structural characterization[33] of Cr-doped Bi_2Se_3 thin films indicate that bismuth substitution sites are strongly preferred by chromium.

The effect of Cr doping on the electronic structure of Bi_2Se_3 can be evaluated by comparing the electronic states near the Fermi level (E_F) of $Bi_{1.993}Cr_{0.007}Se_3$ (Fig. 4(a) and (b)) and Bi_2Se_3 Fig. 4(c) and (d)).

Fig. 4(a) and (c) show the two-dimensional (2D) energy-momentum intensity maps and Fig. 4(b) and (d) the corresponding energy distribution curves (EDCs). In the case of Bi_2Se_3, as expected,[34] there are linearly dispersing states (*i.e.* the TSSs) crossing at $k_{\parallel} = 0$ with a Dirac point (DP) at 0.31 eV BE. The small amount of Cr in $Bi_{1.993}Cr_{0.007}Se_3$ produces notable changes near the DP. An apparent energy gap opening of ~50 meV is visible on the 2D map (Fig. 4(a)) as well as in the EDCs (Fig. 4(b)). The electronic structure of $Bi_2Cr_4Se_9$ (Fig. S6, measured on the crystallite of Fig. S2, ESI†) clearly shows a trivial insulating behavior of the compound with visible non-dispersive bands originating from the Cr 3d electronic states.

A gap opening in Cr-doped of $Bi_{2-x}Cr_xSe_3$ films was found, at *RT* and T = 15 K, to be ~50 meV and 100 meV, for x = 0.05 and x = 0.16, respectively, and in ref. 23, 5 meV, 35 meV and 100 meV, at T = 10 K, for x = 0.02, 0.1 and 0.2, respectively, in ref. 29. It is worth noting that the Cr concentration of these films is higher than that of the Cr-doped Bi_2Se_3 bulk studied here, but the effects on the TSS are similar.

The mechanism leading to a gap opening on the TSS when Cr magnetic impurities are present on the surface and inside Bi_2Se_3, is still not completely clear. The gap observed in ref. 29 at T = 10 K is attributed to ferromagnetic ordering at a temperature below Curie temperature, T_C = 35 K. In ref. 23 the gap is observed at both T = 15 K and RT and attributed to

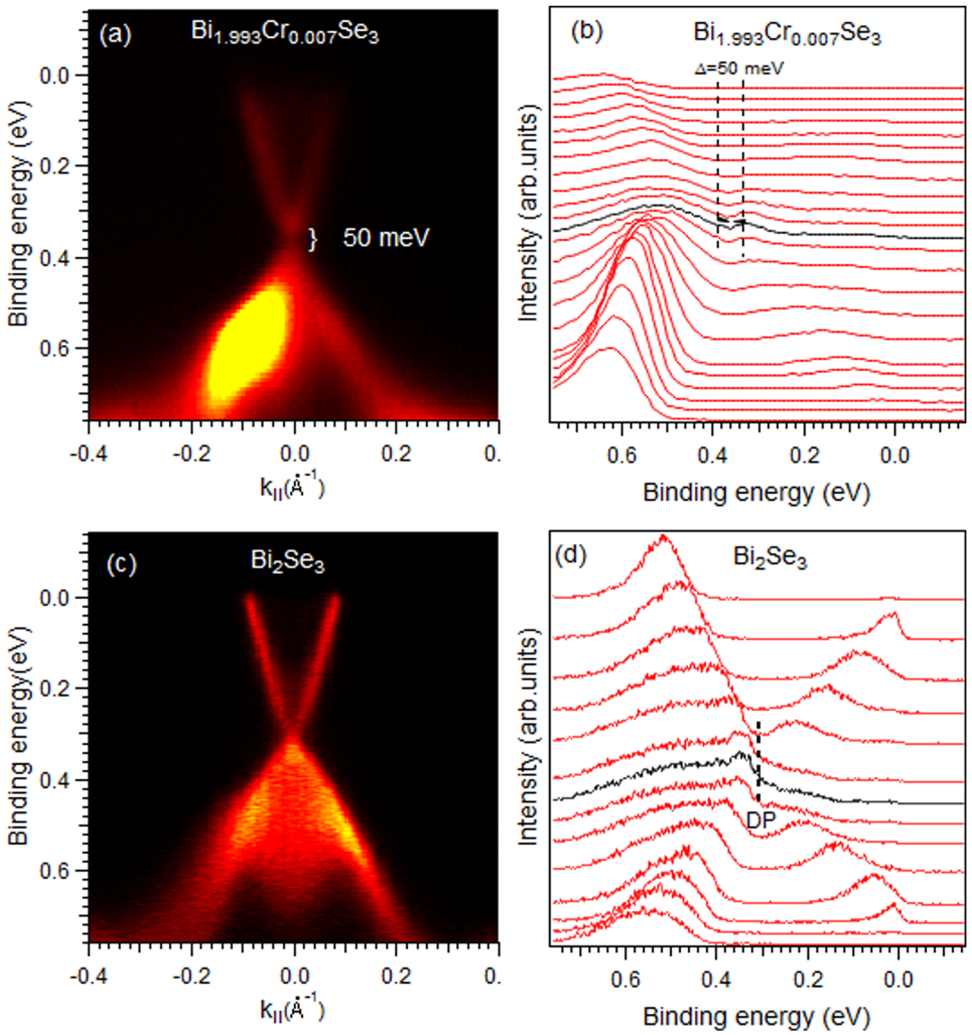

Fig. 4 Electronic band structure measured near E_F by means of ARPES on $Bi_{1.993}Cr_{0.007}Se_3$ and Bi_2Se_3 sample. 2D intensity map (a) is measured with $h\nu$ = 45 eV while (c) is measured with $h\nu$ = 50 eV. The EDCs of maps (a) and (c) are reported in (b) and (d) respectively. The black spectra in (b) and (d) represents the EDC at Γ point. $k_{||}$ = 0 $Å^{-1}$ represents the Γ point.

impurity states that strongly modify the Dirac cone of the material.[23,24] It is also known that Cr atoms deposited on the surface of Bi_2Se_3 do not induce a gap opening at cryogenic temperatures or at RT.[23,35] This is interpreted as due to the absence of a long-range out-of-plane ferromagnetic order. Calculations have shown that the depth of penetration of TSS into the interior of a TI is about 10 atomic layers.[29] Therefore, magnetic impurities deposited only on the surface of a TI, could affect only marginally the properties of the TSS, which extends significantly in the sub-surface region.[23,35] In our study, Cr impurities are also dispersed in the subsurface layers and can modify significantly the spectral properties of the TSS with respect to the pure Bi_2Se_3 case, as observed by ARPES in Fig. 4.

In conclusion, we have achieved extreme dilution of Cr at the surface and in the bulk of Bi_2Se_3 by phase separation from the melt, in which the Cr concentration is far above its solubility in Bi_2Se_3. Using this method, we obtain large (~500 μm × 500 μm) and chemically homogeneous $Bi_{1.993}Cr_{0.007}Se_3$ crystals, which can be easily separated from secondary phases ($Bi_2Cr_4Se_9$ and $BiCrSe_3$). ARPES measurements on the diluted $Bi_{1.993}Cr_{0.007}Se_3$ phase showed that very low Cr dopant concentration can affect the integrity of the TSS of Bi_2Se_3 as observed in the case of Cr-doped Bi_2Se_3 thin films for higher Cr concentrations.[23,24] It is difficult to determine whether the induced gap is due to magnetism-related symmetry breaking, the presence of a resonance state or a combination of these factors. With our work we have demonstrated the growth by the Bridgman method of a topological insulator in the bulk form with homogeneously distributed magnetic atoms. We have shown that the surface of our crystals has the same electronic structure of Cr-doped Bi_2Se_3 thin films. Our synthesis procedure is an alternative method to the current thermodynamically unstable or metal-stable phases obtained by thin film growth methods. The results obtained will have an impact on both the study of the fundamental properties and the applications of TI doped with magnetic and non-magnetic 3d, 4d and 5d transition metals and rare earth metals. Indeed, our study has shown the importance of phase equilibrium considerations in the synthesis of doped bulk TI materials using conventional methods such as the Bridgman method.

Starting from a supersaturated melt with dopants, through a process of crystallization and phase separation, it is possible to prepare the single-crystal composition with dopant at a concentration exactly corresponding to the solubility limit without introducing impure phases, allowing accurate study of the electronic, magnetic and transport properties, thus opening up their potential applications.

Data availability

The data supporting this article have been included in the article and in the ESI.†

Conflicts of interest

There are no conflicts to declare.

Acknowledgements

The authors acknowledge financial support from the Slovenian Research and Innovation Agency (research core funding No. P2-0412 and project funding No. J2-3039). We acknowledge EUROFEL-ROADMAP ESFRI of the Italian Ministry of University and Research. We acknowledge Elettra Sincrotrone Trieste for providing access to its synchrotron radiation facilities.

References

1 Y. Tokura, K. Yasuda and A. Tsukazaki, *Nat. Rev. Phys.*, 2019, **1**, 126–143.
2 J. Sun and D. J. Singh, *J. Appl. Phys.*, 2017, **121**, 064301–064306.
3 D. Li, J. Lao, C. Jiang, C. Luo, R. Qi, H. Lin, R. Huang, G. I. N. Waterhouse and H. Peng, *Int. J. Hydrogen Energy*, 2019, **44**, 30876–30884.
4 S. Jayachitra, P. Ravi, P. Murugan and M. Sathish, *J. Colloid Interface Sci.*, 2022, **605**, 871–880.
5 L. Xiao, A. Zhu, Q. Xu, Y. Chen, J. Xu and J. Weng, *ACS Appl. Mater. Interfaces*, 2017, **9**, 6931–6940.
6 H. Zhang, X. Zhang, C. Liu, S. T. Lee and J. Jie, *ACS Nano*, 2016, **10**, 5113–5122.
7 C. R. Rajamathi, U. Gupta, K. Pal, N. Kumar, H. Yang, Y. Sun, C. Shekhar, B. Yan, S. Parkin, U. V. Waghmare, C. Felser and C. N. R. Rao, *Chem. Phys. Chem.*, 2017, **18**, 2322–2327.
8 Z. Zou, Z. Yu, C. Chen, Q. Wang, K. Zhu, K. Ye, G. Wang, D. Cao and J. Yan, *ACS Nano*, 2023, **17**, 13769–13783.
9 R. Yu, W. Zhang, H.-J. Zhang, S.-C. Zhang, X. Dai and Z. Fang, *Science*, 2010, **329**, 61–64.
10 B. A. Bernevig, C. Felser and H. Beidenkopf, *Nature*, 2022, **603**, 41–51.
11 X. L. Qi, T. L. Hughes and S. C. Zhang, *Phys. Rev. B*, 2008, **78**, 195424.
12 Q. Liu, C. X. Liu, C. Xu, X. L. Qi and S. C. Zhang, *Phys. Rev. Lett.*, 2009, **102**, 156603.
13 G. G. Shabunina, E. V. Kireeva and T. G. Aminov, *Russ. J. Inorg. Chem.*, 1996, **41**, 1496.
14 P. P. J. Haazen, J. B. Laloë, T. J. Nummy, H. J. M. Swagten, P. Jarillo-Herrero, D. Heiman and J. S. Moodera, *Appl. Phys. Lett.*, 2012, **100**, 082404.
15 W. Liu, D. West, L. He, Y. Xu, J. Liu, K. Wang and Y. Wang, *ACS Nano*, 2015, **9**, 10237.
16 A. I. Figueroa, G. Van Der Laan, L. J. Collins-McIntyre, G. Cibin, A. J. Dent and T. Hesjedal, *J. Phys. Chem. C*, 2015, **119**, 17344–17351.
17 J. M. Zhang, W. Zhu, Y. Zhang, D. Xiao and Y. Yao, *Phys. Rev. Lett.*, 2012, **109**, 266405.
18 C. Z. Chang, P. Tang, Y. L. Wang, X. Feng, K. Li, Z. Zhang, Y. Wang, L. L. Wang, X. Chen, C. Liu, W. Duan, K. He, X. C. Ma and Q. K. Xue, *Phys. Rev. Lett.*, 2014, **112**, 109901.
19 L. J. Collins-Mcintyre, S. E. Harrison, P. Schönherr, N. J. Steinke, C. J. Kinane, T. R. Charlton, D. Alba-Veneroa, A. Pushp, A. J. Kellock, S. S. P. Parkin, J. S. Harris, S. Langridge, G. Van Der Laan and T. Hesjedal, *EPL*, 2014, **107**, 57009.
20 F. Yang, Y. R. Song, H. Li, K. F. Zhang, X. Yao, C. Liu, D. Qian, C. L. Gao and J. F. Jia, *Phys. Rev. Lett.*, 2013, **111**, 176802.
21 M. G. Vergniory, M. M. Otrokov, D. Thonig, M. Hoffmann, I. V. Maznichenko, M. Geilhufe, X. Zubizarreta, S. Ostanin, A. Marmodoro, J. Henk, W. Hergert, I. Mertig, E. V. Chulkov and A. Ernst, *Phys. Rev. B: Condens. Matter Mater. Phys.*, 2014, **89**, 165202.
22 Y. L. Chen, J. H. Chu, J. G. Analytis, Z. K. Liu, K. Igarashi, H. H. Kuo, X. L. Qi, S. K. Mo, R. G. Moore, D. H. Lu, M. Hashimoto, T. Sasagawa, S. C. Zhang, I. R. Fisher, Z. Hussain and Z. X. Shen, *Science*, 2010, **329**, 659–662.
23 T. Yilmaz, W. Hines, F. C. Sun, I. Pletikosić, J. Budnick, T. Valla and B. Sinkovic, *Appl. Surf. Sci.*, 2017, **407**, 371–378.
24 T. Yilmaz, G. D. Gu, E. Vescovo, K. Kaznatcheev and B. Sinkovic, *Phys. Rev. Mater.*, 2020, **4**, 024201.
25 A. M. Black-Schaffer and A. V. Balatsky, *Phys. Rev. B: Condens. Matter Mater. Phys.*, 2012, **85**, 121103(R).
26 N. Kumar, S. N. Guin, K. Manna, C. Shekhar and C. Felser, *Chem. Rev.*, 2021, **121**, 2780–2815.
27 P. Cermak, P. Ruleova, V. Holy, J. Prokleska, V. Kucek, K. Palka, L. Benes and C. Drasar, *J. Solid State Chem.*, 2018, **258**, 768–775.
28 D. A. Barlow, J. K. Baird and C. H. Su, *J. Cryst. Growth*, 2004, **264**, 417–423.
29 X. F. Kou, W. J. Jiang, M. R. Lang, F. X. Xiu, L. He, Y. Wang, Y. Wang, X. X. Yu, A. V. Fedorov, P. Zhang and K. L. Wang, *J. Appl. Phys.*, 2012, **112**, 063912.
30 L. A. Walsh, C. M. Smyth, A. T. Barton, Q. Wang, Z. Che, R. Yue, J. Kim, M. J. Kim, R. M. Wallace and C. L. Hinkle, *J. Phys. Chem. C*, 2017, **121**, 23551–23563.
31 M. Shenasa, S. Sainkar and D. Lichtman, *J. Electron Spectrosc. Relat. Phenom.*, 1986, **40**, 329–337.
32 A. Kukay, *Chromium Selenide Synthesis And Characterization*, MS thesis, University of North Dakota, 2019, **https://commons.und.edu/theses/2467**.
33 A. Ghasemi, D. Kepaptsoglou, L. J. Collins-McIntyre, Q. Ramasse, T. Hesjedal and V. K. Lazarov, *Sci. Rep.*, 2016, **6**, 2–6.
34 Z. R. Benher, S. Gardonio, M. Fanetti, P. Moras, A. K. Kundu, C. Bigi and M. Valant, *J. Mater. Chem. C*, 2021, **9**, 3058–3064.
35 E. Wang, P. Tang, G. Wan, A. V. Fedorov, I. Miotkowski, Y. P. Chen, W. Duan and S. Zhou, *Nano Lett.*, 2015, **15**, 2031–2036.